Distributed Current Sensing Technology for protection and Fault Location Applications in HVDC networks

Dimitrios Tzelepis†, Adam Dyśko†, Campbell Booth†, Grzegorz Fusiek†, Pawel Niewczas†, Tzu Chief Peng†
†*Department of Electronic & Electrical Engineering, University of Strathclyde, Glasgow, UK*
dimitrios.tzelepis@strath.ac.uk, a.dysko@strath.ac.uk, campbell.d.booth@strath.ac.uk
g.fusiek@strath.ac.uk, p.niewczas@strath.ac.uk, tzuchieh.peng@strath.ac.uk

***Keywords*—Multi terminal direct Current, Differential protection, Travelling waves, Distributed sensing**

Abstract

This paper presents a novel concept for a distributed current optical sensing network, suitable for protection and fault location applications in High Voltage Multi-terminal Direct Current (HV-MTDC) networks. By utilising hybrid Fibre Bragg Grating (FBG)-based voltage and current sensors, a network of current measuring devices can be realised which can be installed on an HV-MTDC network. Such distributed optical sensing network forms a basis for the proposed 'single ended differential protection' scheme. The sensing network is also a very powerful tool to implement a travelling-wave-based fault locator on hybrid transmission lines, including multiple segments of cables and overhead lines. The proposed approach facilitates a unique technical solution for both fast and discriminative DC protection, and accurate fault location, and thus, could significantly accelerate the practical feasibility of HV-MTDC grids. Transient simulation-based studies presented in the paper demonstrate that by adopting such sensing technology, stability, sensitivity, speed of operation and accuracy of the proposed (and potentially others) protection and fault location schemes can be enhanced. Finally, the practical feasibility and performance of the current optical sensing system has been assessed through hardware-in-the-loop testing.

1. Introduction

Power transmission based on High Voltage Direct Current (HVDC) networks is expected to be the favoured technology for massive integration of renewable energy sources and the realisation of European and Asian supergrids [1], [2]. DC-side faults are the greatest challenge when it comes to the realisation of HVDC-based grids, due to the fact that large inrush currents escalating over a short period of time [3].

After the occurrence of a DC-side fault on a HVDC transmission system, dedicated protection schemes are expected to minimise its adverse effects, by initiating fault-clearing actions such as selective tripping of circuit breakers. Following the fast and successful fault clearance, the next important action is the accurate calculation of its distance with regards to feeder's length. This is of major importance as it will permit faster system restoration, diminish the power outage time, and therefore enhance the overall reliability of the system.

Distributed sensing in power systems is an advanced, cutting-edge technology (with numerous operational, technical and economic benefits) which aims to accelerate power system protection and control applications [4]–[11]. In this paper the work conducted in [4], [5] is further demonstrated to highlight the technical merits when adopted for protection and fault location applications in HVDC networks.

2. Modelling

For the studies presented in this paper, a five terminal Multi-Terminal Direct Current MTDC grid (illustrated in Figure 1) has been developed in Matlab/Simulink. The system architecture has been adopted from the Twenties Project case study on DC grids. There are five 400-level, Modular Multilevel Converters (MMCs) operating at ± 400 kV (in symmetric monopole configuration), Hybrid Circuit Breakers (HbCBs), and current limiting inductors at each transmission line end.

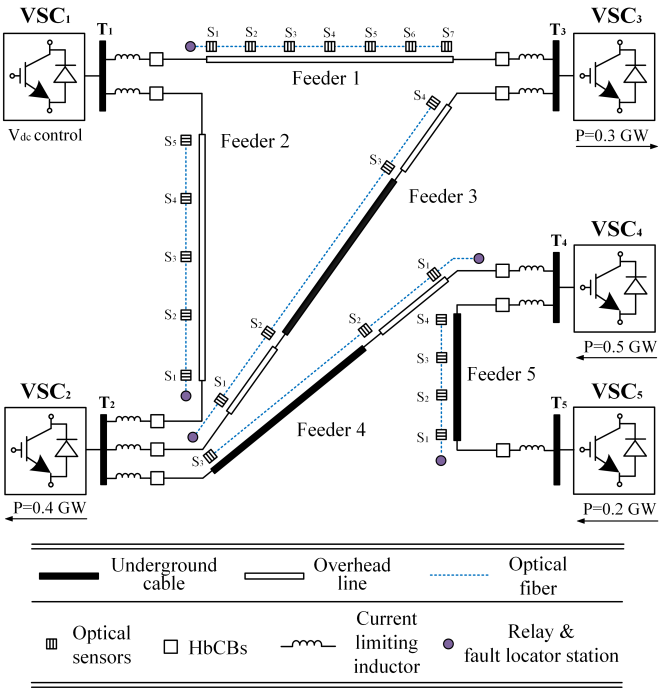

Figure 1: Five terminal MTDC grid.

The MTDC network includes uniform feeders but also hybrid feeders comprising of both overhead lines (OHLs) and underground cables (UGCs). It should be noted that feeders 1, 3 and 5 will be utilised for demonstrating the proposed HVDC protection scheme while feeders 3 and 4 will be used to demonstrate a fault location scheme. On each uniform feeders (i.e. feeders 1, 2 and 5), optical sensors are installed to accurately measure DC current every 30 km including the terminals. On hybrid feeders optical sensors are installed

at junctions and feeder terminals. The measurements are captured and processed at each line terminal ('relay & fault locator station'). Transmission lines have been modelled by adopting distributed parameter model, while for the DC breaker a hybrid design by ABB [12] has been considered. The parameters of the AC/DC network components are described in detail in Table 1 and line parameters in Table 2.

TABLE 1: MTDC network parameters.

Parameter	Value
DC voltage [kV]	± 400
DC inductor [mH]	150
AC frequency [Hz]	50
AC short circuit level [GVA]	40
AC voltage [kV]	400

TABLE 2: Lengths of OHLs and UGCs Included in MTDC Case Study Grid.

HTM-1	OHL: 180 km
HTM-2	OHL: 120 km
HTM-3	OHL-a: 65 km, UGC: 180 km, OHL-b: 35 km
HTM-4	UGC: 50 km, OHL: 130 km
HTM-5	UGC: 90 km

3. Single-ended differential protection scheme

3.1. Protection algorithm

The single-ended differential protection algorithm is illustrated using a flowchart in Figure 2 [4].

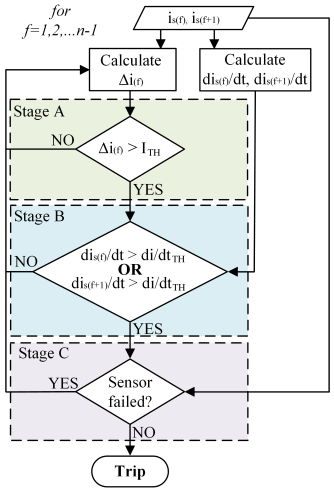

Figure 2: Protection algorithm of single-ended differential protection scheme.

Using the measurements of two consecutive sensors, the algorithm starts by calculating a series of differential currents given by

$$\Delta i_{(f)}(t) = i_{s(f)}(t - \Delta t) - i_{s(f+1)}(t) \qquad (1)$$

where $\Delta i_{(f)}(t)$ is the f-th differential current derived using the currents $i_{s(f)}$, $i_{s(f+1)}$ measured at two adjacent sensors f and $f+1$ respectively ($f = 1, 2, ..., n-1$) and Δt the amount of time compensation due to propagation delays.

The protection logic has three stages. The first stage (Stage A) is a comparison of differential current $\Delta i_{(f)}(t)$ with a predefined threshold value I_{TH}. When the threshold I_{TH} is exceeded for a differential current $\Delta i_{(f)}$, the protection algorithm will inspect the historical data of $di_{s(f)}/dt$ and $di_{s(f+1)}/dt$ using a short time window $\Delta t_w = 0.2$ ms. If any of the historical values of the derivatives $di_{s(f)}/dt(t - \Delta t_w)$ or $di_{s(f+1)}/dt(t - \Delta t_w)$ exceed a predefined threshold di/dt_{TH}, the criterion for Stage B is fulfilled. This stage will ensure stability of protection to any kind of short disturbance. The final stage (Stage C) is included to ensure that the operation of the protection scheme does not originate from any sensor failure. If no sensor failure is detected, Stage C initiates a tripping signal to the corresponding CB.

The resulting key advantages of the proposed single-ended differential protection include high speed of operation, enhanced reliability and superior stability. Detailed evaluation of the method can be found in [4].

3.2. Simulation results

The protection performance of the proposed scheme has been tested for numerous faults along the MTDC case study grid (fault have been applied on Feeders 1, 2 and 5). It should be noted that the protection scheme is based on a sampling rate of 5 kHz.

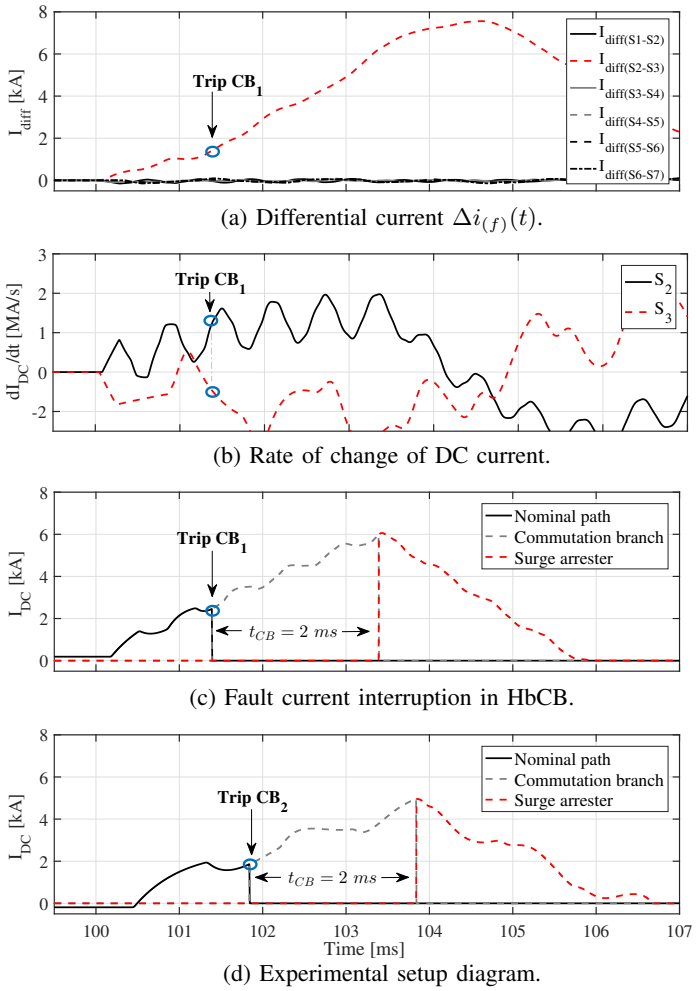

(a) Differential current $\Delta i_{(f)}(t)$.

(b) Rate of change of DC current.

(c) Fault current interruption in HbCB.

(d) Experimental setup diagram.

Figure 3: Illustration of pole-to-pole fault at Feeder 1.

Figure 3 illustrates the protection response to an internal fault (initiated at $t = 100$ ms) occurring at 50 km (from

terminal T_1) on Feeder 1. This fault is practically located between sensors S_2 and S_3. As such, the differential current $I_{diff(S2-S3)}$ calculated from the measurements of sensors S_2 and S_3 is increasing rapidly (Figure3a), exceeding the protection threshold, and hence, fulfilling Stage A. Figure 3b demonstrates that prior to the fault detection the rate of change di_{DC}/dt for both currents (sensors S_2 and S_3) is non-zero which indicates the fulfilment of Stage B. A tripping signal is initiated by the third criterion (Stage C), however it is not depicted here due to space limitations. The fault current interruption is depicted in Figure 3c and Figure 3d for both ends of Feeder 1.

The summarised results are presented in Tables 3 and 4 for pole-to-pole and pole-to-ground faults (with ground fault resistances of up to 300 Ω) respectively. It can be demonstrated that in all cases only the required breakers operate, proving high selectivity of the scheme.

TABLE 3: Protection performance results for pole-to-pole faults.

Line	Distance [km]	Breakers operated	Sending end		Receiving end	
			CB trip time [ms]	CB max. current [kA]	CB trip time [ms]	CB max. current [kA]
1	1	CB_1, CB_2	1.329	7.45	2.075	4.07
	90	CB_1, CB_2	1.525	5.12	1.675	5.28
	120	CB_1, CB_2	1.677	5.41	1.525	5.82
	179	CB_1, CB_2	2.074	4.44	1.331	7.07
2	1	CB_3, CB_4	1.327	7.49	1.775	5.17
	25	CB_3, CB_4	1.280	6.47	1.730	5.00
	60	CB_3, CB_4	1.373	5.97	1.524	5.81
	119	CB_3, CB_4	1.774	5.56	1.326	7.06
5	1	CB_9, CB_{10}	1.325	7.33	1.630	5.20
	45	CB_9, CB_{10}	1.376	6.18	1.374	5.73
	89	CB_9, CB_{10}	1.631	5.64	1.330	6.98

TABLE 4: Protection performance results for pole-to-ground faults.

Line	Distance [km]	Breakers operated	Sending end		Receiving end	
			CB trip time [ms]	CB max. current [kA]	CB trip time [ms]	CB max. current [kA]
1	1	CB_1, CB_2	1.382	1.65	2.125	1.05
	90	CB_1, CB_2	1.565	1.40	1.715	1.12
	120	CB_1, CB_2	1.714	1.42	1.567	1.19
	179	CB_1, CB_2	2.128	1.38	1.380	1.43
2	1	CB_3, CB_4	1.377	2.12	1.820	0.98
	25	CB_3, CB_4	1.330	2.03	1.780	1.03
	60	CB_3, CB_4	1.420	1.84	1.566	1.04
	119	CB_3, CB_4	1.830	1.75	1.381	1.22
5	1	CB_9, CB_{10}	1.400	0.81	1.700	1.08
	45	CB_9, CB_{10}	1.415	0.74	1.414	1.13
	89	CB_9, CB_{10}	1.680	0.86	1.383	1.25

4. Enhanced Fault Location for Hybrid Feeders

Fault location in the case of hybrid feeders is not a straightforward task and hence travelling waved based methods cannot be directly applied. This arises from the fact that in such feeders, the speed of electromagnetic wave propagation is not uniform, additional reflections/refractions are generated at the junction points, and there is an increased difficulty in recognising the faulted segment. The fault location scheme presented in this paper [5] utilises the principle of travelling waves applied to a series of captured waveforms acquired from current sensors installed along hybrid feeders (see Feeders 3 and 4 in Figure 1).

4.1. Fault location algorithm

The proposed fault location algorithm consists of three stages as illustrated in Figure 4.

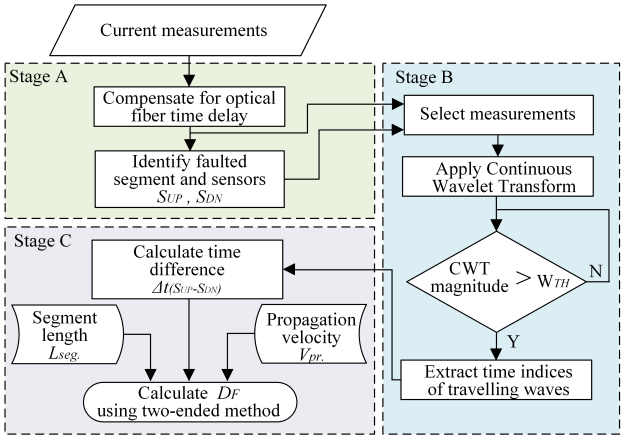

Figure 4: Protection algorithm of fault location scheme.

The first stage (Stage A) of the algorithm identifies the faulted segment. This is implemented by calculating the differential current $\Delta i_{(f)}$ for every pair of adjacent sensors (similarly to equation (1)). When a fault occurs between two sensors, the differential current $\Delta i_{(f)}$ calculated from measurements acquired from those sensors reaches much higher level than the current captured from any other adjacent pair (this was also demonstrated in Figure 3a). As such, by identifying the highest differential current, the faulted segment is identified. At this point the algorithm will produce two outputs: S_{up} and S_{dn} for the sensors located upstream downstream to the fault respectively.

Since the faulted segment has been identified in Stage A, post-fault current measurements corresponding to sensors S_{up} and S_{dn} are utilised at the next stage (Stage B). These measurements are used to calculate the precise time of travelling wave arrival at faulted segment terminals (where the sensors S_{up} and S_{dn} are located). The wave detection is implemented by applying Continuous Wavelet Transform (CWT) on the available current measurements. The wavelet transform of a function $i(t)$ can be expressed as the integral of the product of $i(t)$ and the daughter wavelet $\Psi^*_{a,b}(t)$ given by

$$WT_\psi i(t) = \int_{-\infty}^{\infty} i(t) \underbrace{\frac{1}{\sqrt{\alpha}}\Psi\left(\frac{t-b}{a}\right)}_{\text{daughter wavelet } \Psi^*_{a,b}(t)} dt \qquad (2)$$

The daughter wavelet $\Psi^*_{a,b}(t)$ is a scaled and shifted version of the mother wavelet $\Psi_{a,b}(t)$. Scaling is implemented by α which is the binary dilation (also known as scaling factor) and shifted by b which is the binary position (also known as shifting or translation). Finally, Stage B will produce two outputs: $t_{S_{up}}$ and $t_{S_{dn}}$ which correspond to the time index of the initial travelling wave at the faulted segment terminals.

In Stage C of the proposed algorithm, the actual fault location D_F of the faulted segment is calculated by adopting the conventional, two-ended fault location approach given by

$$D_F = \frac{L_{seg} - \Delta t_{(S_{up}-S_{dn})} \cdot v_{prop}}{2} \qquad (3)$$

where $\Delta t_{(S_{up}-S_{dn})}$ is the time difference of the initial travelling waves at sensing locations S_{up} and S_{dn}, and v_{prop} is the propagation velocity of the faulted segment (the propagation

velocity has been calculated according to the conductor geometry).

4.2. Simulation results

In order to validate the performance of the proposed scheme, pole-to-pole and pole-to-ground faults have been applied on Feeders 3 and 4 (see Figure 1) at various distances at all segments. Since the accuracy of travelling wave-based techniques depend on sampling frequency, for the studies presented in this paper a sampling rate of 135 kHz has been assumed. This frequency corresponds to the resonant frequency of optical sensors and the signal acquisition at this rate can be practically achieved by employing Arrayed Waveguide Grating (AWG) interrogators [13]. The values of fault location estimation error have been reported according to formula (4)

$$error\ [\%] = \frac{D_F - A_{DF}}{L_{f-seg}} \cdot 100\% \tag{4}$$

where D_F is the calculated fault distance, A_{DF} is the actual fault distance and L_{f-seg} the total length of the faulted segment.

The results are presented in Tables 5 and 6 for pole-to-pole and pole-to-ground faults respectively. The average, minimum and maximum errors observed for pole-to-pole faults correspond to 0.3644 %, 0.0012 % and 1.4625 % respectively. For pole-to-ground faults these errors correspond to 0.3955 %, 0.0390 % and 1.3214 % respectively. It can be also seen that the faulted segment has been identified correctly in 100 % of the cases for both types of faults (see 'Reported sensors' column in Tables 5 and 6).

The impact of noise in measurements, mother wavelet, scaling factor α and network components on the accuracy of the proposed fault location scheme, are exhaustively analysed and reported in [5].

TABLE 5: Segment identification and fault location results for pole-to-pole faults.

Feeder	Segment	Fault distance [km]	Reported sensors S_{UP}	Reported sensors S_{DN}	Reported fault location [km]	Error [%]
3	OHL-a	12.4	S_1	S_2	11.7669	-0.9740
3	OHL-a	35.0	S_1	S_2	35.7736	1.1902
3	OHL-a	42.0	S_1	S_2	42.3209	0.4937
3	OHL-a	50.1	S_2	S_3	51.0506	1.4625
3	OHL-a	57.3	S_2	S_3	57.5979	0.4583
3	UGC	10.0	S_2	S_3	9.6516	-0.1936
3	UGC	39.7	S_2	S_3	39.9929	0.1627
3	UGC	56.7	S_2	S_3	56.8493	0.0829
3	UGC	95.0	S_2	S_3	95.0569	0.0316
3	UGC	100.0	S_2	S_3	99.5519	-0.2489
3	UGC	103.0	S_2	S_3	102.9232	-0.0427
3	UGC	161.2	S_2	S_3	161.3584	0.0880
3	UGC	173.0	S_3	S_4	172.5959	-0.2245
3	OHL-b	26.7	S_3	S_4	26.6210	-0.2256
3	OHL-b	30.0	S_3	S_4	29.9337	-0.1893
3	OHL-b	33.7	S_3	S_4	33.8682	0.4806
4	UGC	3.8	S_1	S_2	3.6487	-0.3027
4	UGC	13.2	S_1	S_2	13.2006	0.0012
4	UGC	29.10	S_1	S_2	29.4950	0.7900
4	UGC	46.6	S_1	S_2	46.3513	-0.4973
4	OHL	29.0	S_2	S_3	28.9899	-0.0077
4	OHL	53.5	S_2	S_3	52.9966	-0.3872
4	OHL	74.0	S_2	S_3	73.7297	-0.2079
4	OHL	110.2	S_2	S_3	109.7398	-0.3540
4	OHL	125.0	S_2	S_3	125.0168	0.0129

TABLE 6: Segment identification and fault location results for pole-to-ground faults ($R_f = 500\ \Omega$).

Feeder	Segment	Fault distance [km]	Reported sensors S_{UP}	Reported sensors S_{DN}	Reported fault location [km]	Error [%]
3	OHL-a	8.1	S_1	S_2	8.4933	0.6051
3	OHL-a	23.8	S_1	S_2	24.5979	1.2276
3	OHL-a	35.6	S_1	S_2	35.7736	0.2671
3	OHL-a	46.5	S_1	S_2	46.6858	0.2858
3	OHL-a	55.5	S_1	S_2	55.4155	-0.1300
3	UGC	8.8	S_2	S_3	8.5278	-0.1512
3	UGC	12	S_2	S_3	11.8991	-0.0561
3	UGC	33	S_2	S_3	33.2504	0.1391
3	UGC	56.4	S_2	S_3	56.2874	-0.0626
3	UGC	100	S_2	S_3	100.1138	0.0632
3	UGC	144.3	S_2	S_3	144.5021	0.1123
3	UGC	156	S_2	S_3	155.7396	-0.1447
3	UGC	165.7	S_2	S_3	165.8534	0.0852
3	UGC	177.5	S_2	S_3	177.6528	0.0849
3	OHL-b	15.2	S_3	S_4	15.3176	0.3359
3	OHL-b	34	S_3	S_4	33.8682	-0.3765
4	UGC	5.1	S_1	S_2	5.3343	0.4686
4	UGC	28	S_1	S_2	28.3713	0.7425
4	UGC	42	S_1	S_2	42.4182	0.8364
4	UGC	48.5	S_1	S_2	49.1607	1.3214
4	OHL	4	S_2	S_3	2.8008	-0.9225
4	OHL	66	S_2	S_3	66.0912	0.0702
4	OHL	83.5	S_2	S_3	83.5506	0.0390
4	OHL	99	S_2	S_3	98.8276	-0.1326
4	OHL	115.7	S_2	S_3	116.2871	0.4516

5. Hardware Validation of Optical Sensing Technology

5.1. Experimental Setup

In order to prove the principle of the new protection and fault location scheme an experimental set-up has been arranged as shown in Figure 6 (the actual laboratory experiment is shown in Figure 5). For the realisation of such an experimental set-up the following key components were required:

- Four Fibre Bragg Grating optical sensors.
- Four transient voltage suppression diodes.
- Optical fibre.
- SmartScan interrogator.
- PXIe-8106 controller (National Instruments).
- PXIe-6259 data acquisition card (National Instruments).
- Pre-simulated DC fault currents.
- PC.

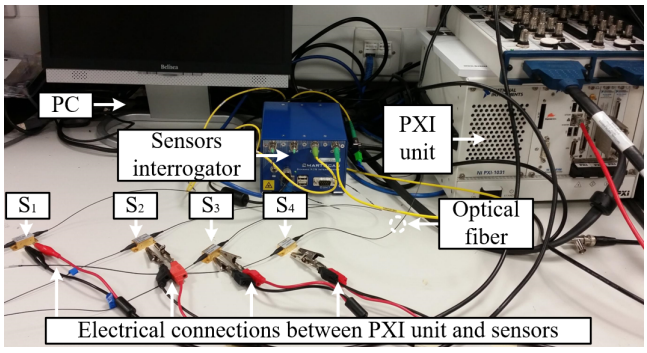

Figure 5: Laboratory experimental arrangement.

For the practical implementation of the proposed schemes, pre-simulated fault currents at corresponding four sensing locations have been generated and stored locally to a PC. For the proposed single-ended differential protection scheme, the model of Feeder 5 has been utilised with one fault placed at 50 km (see Figure 6a). For testing the proposed fault location

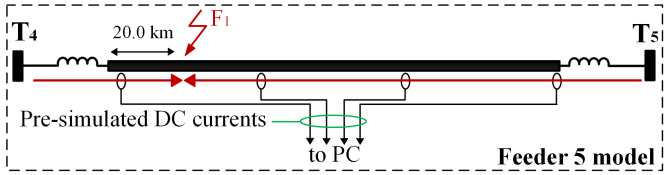

(a) Feeder 5 model.

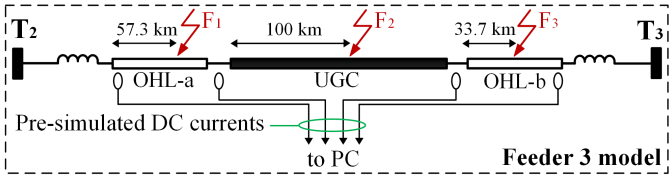

(b) Feeder 3 model.

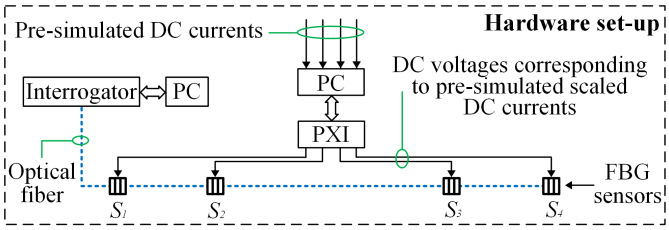

(c) Optical sensing setup.

Figure 6: Laboratory arrangement diagram.

scheme, the model of Feeder 3 has been utilised (see Figure 6b). The pre-simulated fault currents were used to generate replica voltage traces using the data acquisition card. Such voltage waveforms were physically injected to optical sensors and the corresponding data were captured at 5 kHz from the optical interrogator. The sampled data were then stored on a PC for post-processing. Further technical details with regards to the design, operation and installation of optical sensors can be found in [4], [5].

5.2. Experimental results

The measured response of the optical sensors and the protection system to fault at Feeder 5 is illustrated in Figure 7. The recorded DC voltages were used to calculate the differential voltage Δv (corresponding to differential current $\Delta i_{(f)}$ described in equation (1)) which is depicted in Figure 7a. It is evident that the differential voltage between sensors S_1 and S_2 reaches high values which can be easily detected by a voltage threshold. The corresponding rate of change of voltage dV_{dc}/dt of the measurements captured from sensors S_1 and S_2 stay high within a 0.2 ms time window. The entire response of the system is of great resemblance to simulation-based results and hence the protection scheme can be considered practically feasible.

The experimental results related to the proposed fault location scheme (i.e. experimental arrangement shown in Figure 6b) are summarised in Table 7, where they are also compared with the simulation-based results. Due to the reduced sampling rate (i.e. 5 kHz), the resulting accuracy of the experimentally-calculated fault location is notably lower. The sampling frequency has a significant impact on the CWT and the extraction of time difference $\Delta t_{(S_{up}-S_{dn})}$ which is utilised in equation (3) for the calculation of fault distance. This can be further justified from the values of time difference $\Delta t_{(S_{up}-S_{dn})}$ exacted for each fault case, as shown in

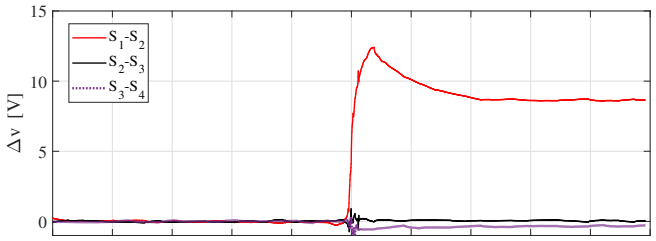

(a) Differential voltage Δv.

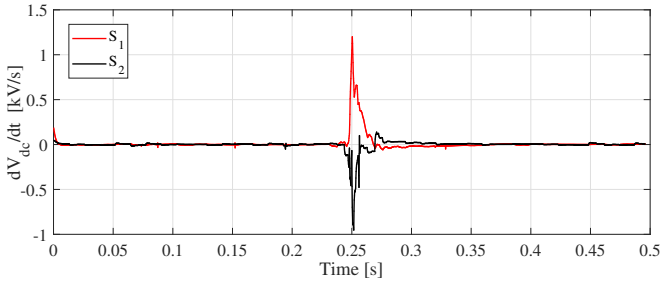

(b) Rate of change of DC voltage Δv.

Figure 7: Optical and protection system response for pre-simulated fault at Feeder 5.

Table 7. With regards to faulted segment, the reported sensors S_{up} and S_{dn} demonstrate that it has been identified correctly at all cases. It should be noted that the resulting diminished accuracy is due to the reduced sampling rate, determined by the available interrogation system. However, the assumed sampling frequency of 135 kHz is practically achievable with other, commercially available equipment.

TABLE 7: Comparison of experimental and simulations results.

Faults		F1	F2	F3
Error [%]	Sim.	0.4583	-0.2489	0.4806
	Exp.	-1.3254	-1.3415	1.0652
$\lvert\Delta t_{(S_{UP}-S_{DN})}\rvert$ $[\mu s]$	Sim.	0.17037	0.12592	0.11110
	Exp.	0.16249	0.10000	0.11250
Reported sensors $S_{UP}-S_{DN}$	Sim.	S_1, S_2	S_2, S_3	S_3, S_4
	Exp.	S_1, S_2	S_2, S_3	S_3, S_4

5.3. Discussion

It has been demonstrated within this paper that optical sensing technology can further enhance the overall performance of protection and fault location applications. This has been demonstrated for HVDC applications, however such technology has been previously utilised in [6]–[10] for protection and control applications in AC systems. The protection, control and fault location schemes have been realised by the employment of optical current and voltage sensors. Such sensors have been designed and manufactured based on magneto-optical constructions based on fibre coils, extrinsic magnetostrictive materials bonded to fibre strain sensors.

In this paper, optical sensors have been used for two different applications namely protection and fault location. The schemes developed for these two application have been designed and tested separately. For example, for the proposed protection scheme, the sensors have been interrogated at a sampling rate of 5 kHz, while for the fault location scheme a sampling rate of 135 kHz has been assumed. The

fundamental difference of these two applications is that the protection needs to be run in real-time while for distance to fault estimation off-line computations can be used. Therefore, lower sampling rate (i.e. 5 kHz) is adequate to permit computational efficiency and high speed operation of the protection module. However, for fault location applications higher sampling rates have to be used in order to guarantee sufficient fault location accuracy. Since the two proposed schemes utilise the same sensing architecture, there is no reason why they could not coexist sharing the same fundamental sensing and interrogation hardware, and forming an integrated protection and fault location system. So long as the fault generated waveforms are captured at adequate sampling rate (i.e. in excess of 100 kHz) both protective and fault locating functions could be performed independently in their respective operating time frames. This would satisfy both, the need for high speed of protection operation and high accuracy of fault location. For example, a real-time calculation with operating frame rate in the range of 5 kHz (using down-sampled data) would be adequate for protection, while for fault location a non-real-time post fault calculation could be performed using the stored data acquired at much higher frequency. A circular memory buffer of approximately 100 ms should provide sufficient amount of data to achieve accurate fault position estimation.

For application in electrical power systems, the key technical and economical merits of the utilised distributed sensing technology (compared to other conventional and purely electrical), arise from the fact that the sensors are completely passive and require no power supply at the sensing location. Moreover, there is no need for additional signal processing and communication equipment (i.e. micro-controllers, GPS, etc.) at the location of the sensors (i.e. sensors are interrogated from a single acquisition point, where measurements can be also time-stamped). These technical merits have the potential to enable reduction in the hardware and infrastructure needs (i.e. communications, low voltage power supplies, decoders/encoders, etc.) required for wide-area monitoring applications. It should be also highlighted that over the last decade the cost of optical sensors has been decreased adequately, leading to practical realisation of cheap and high performance transducers. Overall, due to the extensibility and centralised nature of the sensing technology, the capability of distributed sensing is undoubtedly technically beneficial, while in the long-term, it can ultimately lead to reduction of operational and capital expenditure. Since measurements have been made available [14] in standardised sampled value formats (IEC 61850-9-2), it can be considered a ready-to-use technology for substation automation, and for protection and control of electrical networks (from microgrids to large transmission lines).

6. Conclusions

In this paper, a new single-ended differential protection scheme and a fault location scheme for hybrid feeders has been presented. Such schemes were designed for HV-MTDC networks and are based upon the principle of distributed optical sensing. The proposed protection scheme has been found to be highly sensitive, discriminative and fast both for pole-to-pole and pole-to-ground faults. With regards to fault location in hybrid feeders, the proposed travelling wave-based algorithm, has been found to be capable of identifying the faulted segment, while maintaining high accuracy of the fault location estimation across a wide range of fault scenarios. The overall performance of both schemes have been assessed through transient simulation and further validated using small-scale hardware prototypes and hardware-in-the-loop testing. The potential technical and economical benefits of distributed sensing technology have been also discussed within the paper.

7. Acknowledgements

This work was supported by Royal Society of Edinburgh (J M Lessells Travel Scholarship), Synaptec Ltd | Glasgow - UK, the Innovate UK (TSB Project Number 102594) and the European Metrology Research Programme (EMRP) - ENG61. The EMRP is jointly funded by the EMRP participating countries within EURAMET and the European Union.

References

[1] D. Tzelepis, A. O. Rousis, A. Dysko, C. Booth, and G. Strbac, "A new fault-ride-through strategy for MTDC networks incorporating wind farms and modular multi-level converters," *Electrical Power and Energy Systems*, vol. 92, pp. 104–113, November 2017.

[2] D. V. Hertem and M. Ghandhari, "Multi-terminal VSC-HVDC for the european supergrid: Obstacles," *Renewable and Sustainable Energy Reviews*, vol. 14, no. 9, pp. 3156 – 3163, 2010.

[3] D. Tzelepis, S. Ademi, D. Vozikis, A. Dysko, S. Subramanian, and H. Ha, "Impact of VSC converter topology on fault characteristics in HVDC transmission systems," in *IET 8th International Conference on Power Electronics Machines and Drives*, March 2016.

[4] D. Tzelepis, A. Dyko, G. Fusiek, J. Nelson, P. Niewczas, D. Vozikis, P. Orr, N. Gordon, and C. D. Booth, "Single-ended differential protection in MTDC networks using optical sensors," *IEEE Transactions on Power Delivery*, vol. 32, no. 3, pp. 1605–1615, June 2017.

[5] D. Tzelepis, G. Fusiek, A. Dyko, P. Niewczas, C. Booth, and X. Dong, "Novel fault location in MTDC grids with non-homogeneous transmission lines utilizing distributed current sensing technology," *IEEE Transactions on Smart Grid*, 2017,'Early Access Articles'.

[6] P. Orr, G. Fusiek, C. D. Booth, P. Niewczas, A. Dyko, F. Kawano, P. Beaumont, and T. Nishida, "Flexible protection architectures using distributed optical sensors," in *Developments in Power Systems Protection, 11th International Conference on*, April 2012, pp. 1–6.

[7] P. Orr, G. Fusiek, P. Niewczas, C. D. Booth, A. Dyko, F. Kawano, T. Nishida, and P. Beaumont, "Distributed photonic instrumentation for power system protection and control," *IEEE Transactions on Instrumentation and Measurement*, vol. 64, no. 1, pp. 19–26, Jan 2015.

[8] P. Orr, C. Booth, G. Fusiek, P. Niewczas, A. Dysko, F. Kawano, and P. Beaumont, "Distributed photonic instrumentation for smart grids," in *Applied Measurements for Power Systems,IEEE International Workshop on*, Sept 2013, pp. 63–67.

[9] G. Fusiek, P. Orr, and P. Niewczas, "Temperature-independent high-speed distributed voltage measurement using intensiometric FBG interrogation," in *IEEE International Instrumentation and Measurement Technology Conference*, May 2015, pp. 1430–1433.

[10] P. Orr, G. Fusiek, P. Niewczas, A. Dyko, C. Booth, F. Kawano, and G. Baber, "Distributed optical distance protection using FBG-based voltage and current transducers," *2011 IEEE Power and Energy Society General Meeting*, pp. 1–5, July 2011.

[11] P. Niewczas and J. R. McDonald, "Advanced optical sensors for power and energy systems applications," *IEEE Instrumentation Measurement Magazine*, vol. 10, no. 1, pp. 18–28, Feb 2007.

[12] M. Callavik, A. Blomberg, J. Hafner, and B. Jacobson, "The hybrid HVDC breaker," in *ABB Grid Systems*, November 2012.

[13] G. Fusiek, P. Niewczas, and J. McDonald, "Feasibility study of the application of optical voltage and current sensors and an arrayed waveguide grating for aero-electrical systems," *Sensors and Actuators A: Physical*, vol. 147, no. 1, pp. 177 – 182, 2008.

[14] Synaptec-Ltd, "Our technology," http://synapt.ec/our-technology, accessed:15-11-2017.